Ceramics International 51 (2025) 43276–43288

Contents lists available at ScienceDirect

Ceramics International

journal homepage: www.elsevier.com/locate/ceramint

Decorated cenosphere surface with bioreduced silver nanoparticles for environmental applications

Magdalena Antonowicz [a,b,*], Jana Kupková [b], Gabriela Kratošová [b], Lenka Klecandová [b,c], Martin Vašina [d,e], Justyna Majewska [f], Michaela Tokarčíková [b], Grazyna Simha Martynková [b]

[a] Department of Biomaterials and Medical Devices Engineering, Faculty of Biomedical Engineering, Silesian University of Technology, Zabrze, 41-800, Poland
[b] Nanotechnology Centre, CEET, VŠB-Technical University of Ostrava, Ostrava, 708 00, Czech Republic
[c] Faculty of Materials Science and Technology, VSB-Technical University of Ostrava, Ostrava, 708 00, Czech Republic
[d] Department of Hydromechanics and Hydraulic Equipment, Faculty of Mechanical Engineering, VŠB-Technical University of Ostrava, Ostrava, 708 00, Czech Republic
[e] Department of Physics and Materials Engineering, Faculty of Technology, Tomas Bata University in Zlín, Zlín, 760 01, Czech Republic
[f] Department of Medical Informatics and Artificial Intelligence, Faculty of Biomedical Engineering, Silesian University of Technology, Zabrze, 41-800, Poland

ARTICLE INFO

Handling Editor: Dr P. Vincenzini

Keywords:
Cenospheres
Acid activation
Silver nanoparticles
Stability and acoustic testing

ABSTRACT

Cenospheres (CF) are hollow spherical particles primarily composed of silica (SiO_2) and alumina (Al_2O_3), known as aluminosilicate ceramic microspheres. In this study, CF were fractionated into the four size ranges (40–80 μm, 80–125 μm, 125–160 μm, 160–200 μm), purified, and activated using piranha solution (PS). Acid treatment activation was followed by the CF functionalization with biosynthesized silver colloidal nanoparticles (AgNPs). Silver integration was confirmed using elemental analysis (5.8–7.1 wt% of Ag), and electron microscopy revealed AgNPs (~45 nm) unevenly distributed and locate at surface defects. X-ray diffraction (XRD) analysis confirmed the presence of quartz and mullite phases in both raw and modified CF, indicating structural stability during processing. Sound absorption tests revealed that while larger CF particles—especially the 160–200 μm fraction—initially demonstrated the highest noise reduction coefficient (NRC), with a maximum NRC of 0.210 at 80 mm powder bed height, the modification with AgNP significantly diminished the dependency of sound absorption performance on particle size. Ag-modified samples showed NRC values, CF with a particle size fraction of 160–200 μm: 0.158, at 80 mm, confirming uniform acoustic performance. Mechanical stiffness, expressed by bulk modulus, increased with both particle size and powder bed density, reaching a maximum of 64.26 MPa for CF_160200_2 PS_Ag. Leaching tests under static, dynamic, and rotation conditions revealed limited silver release, with only slightly increased leaching observed for larger particles under rotation. Silver release from CF_160200_2 PS_Ag was 0.007 wt% (static), 0.008 wt% (dynamic), and 0.010 wt% (rotation). Overall, Ag release remained low, confirming high material stability. These results show that silver-modified CF retain their structural and chemical integrity, offer tunable acoustic and mechanical properties, and show excellent potential for long-term use in environmental remediation, sound insulation, and catalytic applications.

1. Introduction

Cenospheres (CF), also known as fly ash microspheres, are lightweight, hollow spherical particles with thin walls, formed as a by-product coal combustion. As one of the key fractions of coal fly ash, CF are characterized by their low density, regular spherical morphology, and composition dominated by silica (SiO_2) and alumina (Al_2O_3). These unique physical and properties make CF highly attractive for a wide range of industrial applications, including as lightweight fillers, thermal and acoustic insulators, or sorbents, and also in construction, automotive, aerospace, and environmental engineering, where they enhance performance while supporting eco-friendly practices. Their use contributes to reducing industrial waste and material costs, while also enhancing the sustainability of composite materials [1–5].

The composition of CF typically includes 40–60 % silica, 20–40 % alumina, and 5–15 % ferrous compounds, with smaller amounts of minerals such as mullite, quartz, calcite, clay minerals, hydromica, pyrite, and siderite depend on the source and types of coal used [3,6,7]. CF

* Corresponding author. Department of Biomaterials and Medical Devices Engineering, Faculty of Biomedical Engineering, Silesian University of Technology, Zabrze, 41-800, Poland.
E-mail address: Magdalena.Antonowicz@polsl.pl (M. Antonowicz).

https://doi.org/10.1016/j.ceramint.2025.07.067
Received 7 March 2025; Received in revised form 3 July 2025; Accepted 8 July 2025
Available online 8 July 2025

have a regular, spherical shape, with diameter usually ranging from 5 μm to 500 μm [8]. Due to their hollow morphology, CF possess an exceptionally low density (ρ = 350–850 g/cm^3), making them ideal for producing lightweight materials and serving as effective sorbents. Their chemical stability, resistance to various chemicals, and low reactivity further enhance their versatility. Additionally, CF are porous objects that can function as sound absorbing materials [9].

After tailored chemical treatment, the porous nature of CF also significantly boosts their water affinity, making them a promising candidate for applications in wastewater treatment and environmental remediation [10]. The combination of high silica and alumina content with a porous structure enables CF to effectively adsorb heavy metals such as lead (Pb), copper (Cu), cadmium (Cd), and zinc (Zn) from contaminated water sources [11,12].

In recent years, interest in modifying cenospheres (CF) has grown significantly, driven by the need to improve their physical, chemical, and mechanical properties for a wide range of industrial applications. These modifications aim to optimize surface structure, enhance porosity, and adjust chemical composition, thereby increasing the adaptability of CF to various functional environments.

One widely used strategy involves chemical surface treatments—such as acid (HCl) or base (NaOH) etching—which effectively increase surface roughness and specific surface area. As a result, the adsorption capacity of CF for contaminants and heavy metals is greatly enhanced [13]. More advanced methods, such as treatment with piranha solution (a mixture of sulfuric acid and hydrogen peroxide), are particularly effective in removing organic residues and significantly improving surface hydrophilicity. This enhanced surface activity further boosts the performance of CF in sorption and environmental remediation processes [10,14].

Further surface engineering of CF, such as coating them with oxides like silicon dioxide (SiO_2) or aluminum oxide (Al_2O_3), significantly enhances their thermal resistance and chemical stability, particularly in harsh operating environments. In addition to inorganic coatings, functional compounds or nanomaterials can also be introduced to impart specific surface properties. For instance, silane-based coatings not only increase hydrophobicity but also improve interfacial bonding with polymer matrices. Functional groups introduced through silanes—such as amine or epoxy groups—facilitate chemical interactions with surrounding materials, thereby improving compatibility with polymers and reinforcing the mechanical strength of resulting composites [1].

In the context of water purification, CF modified with silver nanoparticles (AgNPs) have shown great promise. These functionalized particles effectively eliminate pathogenic microorganisms, thereby enhancing water quality and reducing risks of biological contamination. Moreover, the catalytic properties of silver nanoparticles facilitate the accelerated degradation of pollutants. Particularly when combined with materials like silica (SiO_2) or alumina (Al_2O_3), enabling faster and more efficient removal of harmful substances. These silver-modified CF also function as effective photocatalysts, expediting the decomposition of organic compounds under light exposure, further broadening their environmental and industrial applications [15,16]. Their high surface area, low density, and synergy with silver nanoparticles allow them to be highly efficient in both adsorption and organic pollutant degradation processes.

Functionalized CF can selectively target specific organic or inorganic pollutants in water treatment applications [17]. For example, magnesia-loaded CF have been used to remove excess fluoride from wastewater, showcasing their utility as a water treatment agent. Several studies demonstrated that CF modified with magnesium chloride ($MgCl_2$) could be used to solidify and extract hazardous liquids and wastes [18]. Markandeya et al. found that CF derived zeolites are not only environmentally friendly and economical but also effective in removing both orange and blue dyes from textile mill effluents [19].

Considering the unique properties of CF in combination with silver nanoparticles (AgNPs) in wastewater treatment, we see a positive benefit in biotechnological reduction of catalytically active metal nanoparticles [20,21]. AgNPs can be prepared relatively easily by bioreduction even from concentrated metal precursor under mild laboratory conditions without the use of user-demanding and expensive equipment and toxic chemicals [22,23]. For the selected bioreduction method, it is important to focus on the repeatability and revealing the reaction mechanism can help in the next step of process optimization.

AgNPs are powerful agents for catalytic degradation of contaminants. Their integration into advanced materials and systems continues to drive innovations in environmental remediation, and sustainable industrial processes Balancing their efficacy with environmental safety and scalability remains a key focus for future development. There are considered several mechanisms of Ag-catalysed degradation. Either AgNPs serve as electron mediators, accelerating redox reactions during pollutant degradation or under light exposure, AgNPs enhance the generation of reactive radicals (e.g., hydroxyl radicals, •OH), which break down contaminants [24]. From the above brief review of the current state of knowledge, we see the meaningful use of CF modified with AgNPs in the field of wastewater treatment and degradation of organic and inorganic pollutants.

In this study, we aimed to develop a functional material by producing AgNP-decorated cenospheres for environmental applications.The process began with acid treatment of the CF to remove surface impurities, ensuring a clean substrate for further treatment. This was followed by surface functionalization, to introduce specific functional groups that enhance the adhesion of silver nanoparticles. A variety of analytical techniques were employed to monitor the decoration process and to evaluate the morphology, composition, and structure of the resulting Ag-modified CF powders.

2. Materials and samples preparation

Cenospheres (CF) from GRES-2 Powerplant, Kazakhstan were selected. The modification of the CF was a multi-step process and included:

1. Cleaning of CF from post-industrial pollution,
2. Sieving of CF on a vibrating sieve to obtain the desired particle size fractions,
3. Chemical surface activation using acid etching,
4. Decoration of CF with silver nanoparticles AgNPs.

The cleaning of the CF was carried out based on our previous work [14]. The thus-prepared CF were fractionated 10 min on a laboratory shaker with an amplitude of 2 mm (Retsch, AS 200, digit cA) with sieves certified at range 40–80 μm, 80–125 μm, 125–160 μm, 160–200 μm (Multiserw Morek, Marcyporęba, Poland). The selected size fractions were subjected to comprehensive physicochemical investigations, including HP: Helium Pycnometry, Fourier-Transform Infrared Spectroscopy (FTIR), X-ray diffraction (XRD), scanning electron microscopy (SEM), and sound absorption measurements. Based on the tests and the efficiency of the sieving process, all fractions were chosen for the preparation of samples with AgNPs. In the first stage, CF were subjected to etching pretreatment in fresh, hot piranha solution (PS). Piranha solution is a strong oxidizing agent that removes most organic residues, metal oxides and carbonates. The mixing concentrated sulfuric acid and hydrogen peroxide produces intensive heat. The dissolving a large amount of organics or another contaminant can cause foaming and smoke release during the mixing procedure. Always work in a fume hood and use personal protective equipment (e.g. lab coat, safety glasses, acid resistant gloves, face shield). The etching solution was prepared from 96 % concentrated H_2SO_4 (CAS: 7664-939-5) and 30 % H_2O_2 (CAS:7722-84-1) in a volumetric ratio 10:1 in solution. The powders of CF were added into the prepared piranha solution and heated to 80 °C for 2h with continuous stirring (350 rpm). Then, samples were washed thoroughly with distilled water and 25 % concentrated NH_3 solution

(CAS: 1336-21-6) in order to adjust pH from pH = 1 to pH = 8. Then, CF were filtrated under reduced pressure and dried at 80 °C overnight. In the second step, bioreduced silver nanoparticles were added to CF. *Verbena officinalis* and *Aloysia citrodora* Palau folium were used for the bioreduction of silver ions to silver nanoparticles (AgNPs) due to their rich phytochemical composition, which serves as a natural reducing agent in green synthesis processes. The polyphenolic compounds present in these plants, such as flavonoids, phenolic acids, and terpenoids, exhibit strong reducing and stabilizing properties, playing a key role in the formation of silver nanoparticles [25]. Lemon Verbena leaf (*Aloysia citrodora Palau folium*) and Verbena top plant (*Verbena officinalis L.*) were obtained from Dary Natury company (PL). Before using the dry plants precursors for the synthesis, they were sterilized using a UV-C Sterilizer S-1080 for 2 min. Silver nitrate $AgNO_3$ (CAS 7761-88-8) was purchased from Mach Chemikalie Company (CR). The 50 g mixture of both Verbena precursors (1:1) was used for simple aqueous extract preparation (1100 cm^3 of 100 °C distilled water). After 10 min of leaching, the plant extract was filtrated using Whatman no. 1 filter paper. To the filtrated plant extract, 60 mmol dm^{-3} aqueous $AgNO_3$ solution in a volumetric ratio 1:1 was added with continuous stirring for 60 min (250 rpm). The addition of the plant extract to aqueous $AgNO_3$ solution turned the initial yellowish solution to greenish-brown indicating the formation of AgNPs after 10 min. This biotechnology was approved to give a well reduced AgNPs with sufficient stabilization by the phytochemicals contained in plant biomass [26,27]. The reduced AgNPs were centrifuged (Rotina 420, Hettich Zentrifugen, Germany, angle rotor, 4-place) for 15 min at 7000 rpm to remove residual silver nitrate solution and stop the post-reactions in a colloidal dispersion. The resulting gel-like AgNPs sample is supposed to be a concentrated nanocrystalline product with approx. 50 wt% of AgNPs and remaining water and stabilizing phytochemicals from the precursors.

The decoration of the CF (cenospheres) was performed as following. Centrifuged concentrated AgNPs were mixed with CF at a weight ratio of 1:5. Distilled water was then added to the combined mass at a ratio of 1:25, and then sonicated for 15 min. The samples prepared in this way were dried at 80 °C overnight. In the following text, the samples of CF are distinguished according to the grain size fraction used (40–80 μm, 80–125 μm, 125–160 μm, 160–200 μm) and further as a control without silver and with silver bioreduced nanoparticles (AgNPs).

3. Characterization methods and testing

The chemical composition was obtained from elemental analysis using X-ray fluorescence spectroscopy Supermini200 wavelength dispersive X-ray fluorescence spectrometer (RIGAKU, Japan). Powder CF (cenospheres) samples were placed freely into polyethylene cups with thin Mylar films.

X-ray diffraction was performed to qualitatively determine the phases present in the samples and confirm the presence of Ag. The X-ray powder diffraction (XRD) analysis for the phase composition was performed using a RIGAKU Ultima IV diffractometer with a scintillation detector, CuKα radiation source, NiKβ filter and a Bragg–Brentano arrangement. The samples were measured at ambient atmospheric pressure using the reflection mode (under conditions 40 kV, 40 mA, 2°/min and 0.1 step). The database used to obtain the qualitative phase analysis was ICDD PDF-2/Release 2022.

The infrared spectra were measured to identify characteristic functional groups in a sample. Single reflection ATR technique with a diamond crystal on infrared spectrometer Nicolet iS50 FT-IR (Thermo Nicolet, USA) was used. The Mid-FTIR spectra were collected in the range from 400 to 4000 cm^{-1}, with resolution 4 cm^{-1}, 32 scans.

CF and AgNPS morphology observations and qualitative analysis of elemental composition were carried out using scanning electron microscopes (SEM) Tescan Vega 4 (Tescan, CR) and JSM-7610F Plus (JEOL, Japan) both equiped with X-ray energy dispersive spectrometer (EDS, Oxford Instruments).

The true density of a substance may be defined as the average mass per unit volume, exclusive of all voids that are not a fundamental part of the molecular arrangement. The true density of the samples was determined using an UltraPyc 1200 helium pycnometer, Quantachrome. The capacity of the measuring chamber was 10 cm^3, and the initial helium pressure was 20 psi. The number of measurements per sample was five.

Sound absorption properties of the investigated loose powders were evaluated using the sound absorption coefficient α, which is expressed as the ratio [28]:

$$\alpha = \frac{E_\alpha}{E_i} \tag{1}$$

where E_α is the absorbed sound energy, and E_i is the total incident sound energy. In general, the ability of materials to absorb sound is influenced by various factors, including the excitation frequency of acoustic waves, material thickness, structure, density, temperature, and humidity. The sound absorption of materials is also characterized by the noise reduction coefficient *NRC*, which evaluates the ability of a sound-absorbing material as a single index. This coefficient is the average of the sound absorption coefficients at 250, 500, 1000, and 2000 Hz, and is defined as follows [29]:

$$NRC = \frac{\alpha_{250} + \alpha_{500} + \alpha_{1000} + \alpha_{2000}}{4} \tag{2}$$

Moreover, the sound absorption properties of the investigated powders were compared using the mean sound absorption coefficient α_m, which was calculated as the arithmetic mean of the sound absorption coefficients across the entire frequency range, i.e., from 250 Hz to 6400 Hz.

The sound absorption measurements can also be used to determine the longitudinal elastic coefficient *K*, and thus the mechanical stiffness of loose powder beds. This coefficient is similar to Young's modulus of elasticity and is given by the following equation [30]:

$$K = c^2 \cdot \rho_b = \left(4 \cdot h \cdot f_{p1}\right)^2 \cdot \rho_b \tag{3}$$

where c is the velocity of the longitudinal elastic wave propagated through a powder bed, ρ_b is the bulk density of a powder material, h is the powder bed height, and f_{p1} is the primary absorption peak frequency.

The frequency dependencies of the normal incidence sound absorption coefficient α of the investigated loose powders in the frequency range of 250–6400 Hz were obtained using the transfer function method ISO 10534-2, which is based on the partial standing wave principle [31]. This method employed a BK 4206 two-microphone acoustic impedance tube in combination with a BK 3560-B-030 signal pulse multi-analyzer and a BK 2706 power amplifier (Brüel & Kjær, Nærum, Denmark). The normal incidence sound absorption coefficient α is then determined from the equations [32]:

$$\alpha = 1 - |r|^2 = 1 - \left|\frac{H_{12} - H_I}{H_R - H_{12}} \cdot e^{-2j \cdot k_0 \cdot x_1}\right|^2 \tag{4}$$

$$H_{12} = \frac{p_2}{p_1} = \frac{e^{j \cdot k_0 \cdot x_2} + r \cdot e^{-j \cdot k_0 \cdot x_2}}{e^{j \cdot k_0 \cdot x_1} + r \cdot e^{-j \cdot k_0 \cdot x_1}} \tag{5}$$

$$H_I = e^{-j \cdot k_0 \cdot (x_1 - x_2)} \tag{6}$$

$$H_R = e^{j \cdot k_0 \cdot (x_1 - x_2)} \tag{7}$$

where r is the normal incidence reflection factor, H_{12} is the complex acoustic transfer function, H_I is the transfer function for the incident wave, H_R is the transfer function for the reflected wave, j is the imaginary unit, k_0 is the wave number, x_1 and x_2 are the distances of the two microphone positions from the reference plane ($x = 0$), and p_1 and p_2 are the complex acoustic pressures at two microphone positions. The sound absorption properties of the studied loose powder beds were

investigated using an acoustic impedance tube with an inside diameter of 29 mm, for various powder bed heights ranging from 5 to 80 mm. Experimental measurements of the normal incidence sound absorption coefficient were conducted at an ambient temperature of 21 °C.

The stability of the prepared decorated CF materials was evaluated by testing the leachability of selected elements. Leachates were prepared by mixing CF with distilled water in a ratio of 1:20. For this purpose, CF were mixed with distilled water at a ratio of 1:20. A static test (S) was performed by placing the mixture in a beaker, while dynamic tests were conducted using a horizontal agitation (H) using shaker device and a rotational overhead agitation with Heidolph Reax 20 shaker (R). All tests were performed for 24h at room temperature. The CF were then removed by filtration and stabilised with HNO_3 (analytical grade, 65 %). Ag, Si, Al, Ca, Fe, K, Mg and Ti were determined using atomic emission spectrometry with inductively coupled plasma (AES-ICP) Spectro Arcos (SPECTRO Analytical Instruments Inc., Germany).

4. Results and discussion

4.1. Characterization of functional properties

Cenospheres (CF) are primarily composed of SiO_2 (50–65 wt%), Al_2O_3 (20–37 wt%), and Fe_2O_3 (1–11 wt%) [33]. Due to their high SiO_2 and Al_2O_3 content, they are often referred to as hollow ceramic aluminosilicate microspheres. The main elements expressed in oxide in raw CF are Al_2O_3 (27–31 wt%) and SiO_2 (57.9–60.1 wt%), along with smaller quantities of other oxides such as CaO, Fe_2O_3, K_2O, MgO, P_2O_5, and TiO_2, are denoted in Table 1. The combined SiO_2 and Al_2O_3 content typically ranges from 85 to 92 %.

Prior to acid treatment with piranha solution, all CF fractions contained 2–3 wt.% Fe_2O_3. The CF fractions sized 40–80 μm and 80–125 μm exhibited relatively high CaO levels at 5.74 and 3.68 wt%, respectively. As shown in Table 1, the acid treatment caused only slight changes in the overall chemical composition of the CF. However, there was a noticeable reduction in the concentrations of Mg and Fe cations, which were removed during the acidification process. Other elements, including P, K, Ca, and Ti, also experienced reductions, even though to a lesser extent.

The leaching of major elements of CF chemical composition, Al and Si, was minimal, as evidenced by the stable quantity ratios of these elements before and after treatment. This suggests that the structural integrity of the aluminosilicate framework is largely preserved during the acid treatment.

The ratio SiO_2/Al_2O_3 is a geochemical indicator of the mineral coal forms, from which the cenospheres are formed [33]. This SiO_2/Al_2O_3 ratio is close to 2 wt% and showed a slight decrease when the CF size is bigger. The aluminosilicate composition of the original and acid treated CF size fractions can be described by the general regression equations $SiO_2/Al_2O_3 = 3.74–0.06\ [Al_2O_3]$ and $SiO_2/Al_2O_3 = 4.98–0.1\ [Al_2O_3]$, respectively (Fig. 1).

After decoration of Ag nanoparticles on the surface of CF, the silver content (determined by XRF analysis) was follows: 5.82 wt% in sample CF4080_2 PS_Ag; 6.12 wt% in CF80125_2 PS_Ag; 7.14 wt% in CF125160_2 PS_Ag and 6.92 wt% in CF160200_2 PS_Ag.

Fig. 2 shows the evaluated phase composition of cenospheres: raw, acid treated and after Ag modification. In the XRD patterns of raw CF were identified as major crystalline phases mullite (M; $3Al_2O_3.2SiO_2$; PDF card No. 01-089-2645) and quartz (Q; SiO_2; PDF card No. 01-085-0797). Moreover, the reflections of calcite (C; $CaCO_3$; PDF card No. 01-086-2334) were observed in raw CF in the finest fractions (40–80 μm and 80–125 μm). A considerable amount of amorphous material was observed in XRD patterns as wide band in the 2θ range between 15 and 30° for all CF samples. Comparison of the XRD patterns of the original CF and those after etching reveals that the phase composition of the CF was largely unaffected by the chemical etching process. The mullite and quartz phases persisted in the CF after acid treatment, owing to their low reactivity [29]. Notably, a new reflection appeared following the acid treatment and subsequent Ag modification, indicating the formation of a new phase. The XRD patterns of CF modified with Ag indicate the presence of mullite, quartz and moreover face-centered cubic Ag crystals (S; PDF card No. 01-071-6549) and chlorargyrite (Ch; AgCl; PDF card No. 00-006-0480).

The FTIR spectra show bands characteristic for cenospheres, see Fig. 3 (see also Figure in attachement). The bands observed at approximately 435 cm^{-1} and 540 cm^{-1} are associated with the vibrations of O-Si-O silicate tetrahedra [34]. Additionally, the stretching vibration of the Si-O-Si bridge in quartz, present in fly ash, is evident at 800 cm^{-1} [35]. The presence of mullite was confirmed by a band at ~916 cm^{-1}, corresponding to aluminum in the octahedral position. However, this band was absent in the smallest CF fraction (40–80 μm) [36].

The SiO_4 vibration is presented by asymmetric in-plane stretching vibration of Si-O tetrahedra at ~1032 cm^{-1} and Si-O(Si) and 1087 cm^{-1}, respectively except the CF 160–200 sample. In this sample the most intensive band is shifted to 1045 cm^{-1} which indicate the gradually increasing amount of quartz in the samples (from CF 40–80 to CF 160–200) with the largest portion of quartz in CF160-200, this phenomenon was described by Mozgawa et al. [35]. The following bands at 874 and 1434 cm^{-1} relate to calcite. The formation of $CaCO_3$ is done by reaction of calcium hydroxide with atmospheric CO_2 - the possible formation of Ca $(OH)_2$ and then $CaCO_3$ is due to significant amount of CaO present in the sample (see XRFS analysis) [35,37]. The amount of calcite decreases with increasing size CF fraction, which is visible at the last fraction CF 160–200, where no calcite bands are detected. The last two bands at 1627 cm^{-1} and ~3390 cm^{-1} arises from OH vibration of adsorbed water [38]. Acid etching of CF leads to removal of calcite (874 cm^{-1} and 1434 cm^{-1}). The OH bands of water (around 3390 cm^{-1}) were also decreased. The most intensive band is shifted to higher value from 1032 to 1036 cm^{-1} (in the case of samples CF 40–80 and CF 80–125) and from 1036/1045 cm^{-1} to 1061 cm^{-1} (in the case of samples CF 125–160 and CF 160–200). The addition of green synthesized Ag nanoparticles into the CF leads to presence of some organic bands in FTIR spectrum, e.g., the band at 3388 cm^{-1} corresponds to O-H functional hydroxyl groups.

Table 1
Chemical composition expressed in oxides of original cenospheres and after piranha solution for different fractions evaluated using XRF method, the highlighted elements are of most noticeable change.

	Al_2O_3	SiO_2	P_2O_5	MgO	K_2O	CaO	TiO_2	Fe_2O_3	SiO_2/Al_2O_3
	wt.%								
CF_4080	27.0	57.9	0.98	0.88	1.35	5.74	1.28	3.06	2.14
CF_4080_2 PS	28.8	64.4	0.75	0.36	1.41	0.81	1.21	1.98	2.24
CF_80125	29.2	58.7	0.79	0.72	1.18	3.68	1.40	2.55	2.01
CF_80125_2 PS	31.1	62.1	0.89	0	1.28	0.85	1.23	1.99	2.00
CF_125160	31.7	60.1	0.96	0.35	1.13	1.15	1.39	2.26	1.90
CF_125160_2 PS	32.5	61.3	0.67	0	1.08	0.82	1.43	1.73	1.90
CF_160200	31.8	58.0	0.85	0.54	1.03	1.57	1.30	2.19	1.82
CF_160200_2 PS	33.3	60.0	0.90	0.23	1.11	0.89	1.25	1.98	1.80

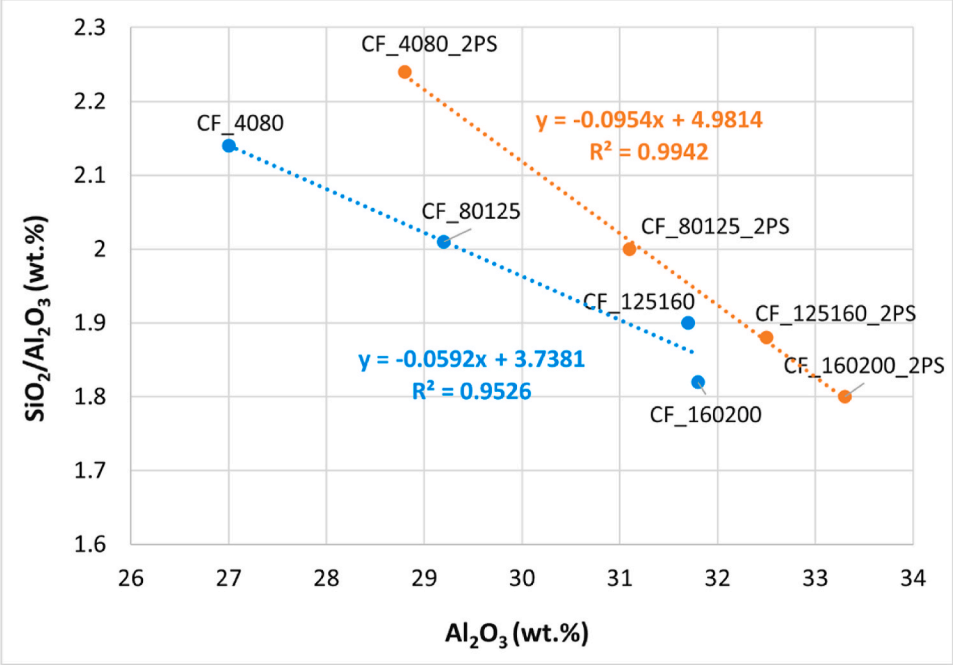

Fig. 1. Dependences of the SiO_2/Al_2O_3 ratio on the Al_2O_3 content.

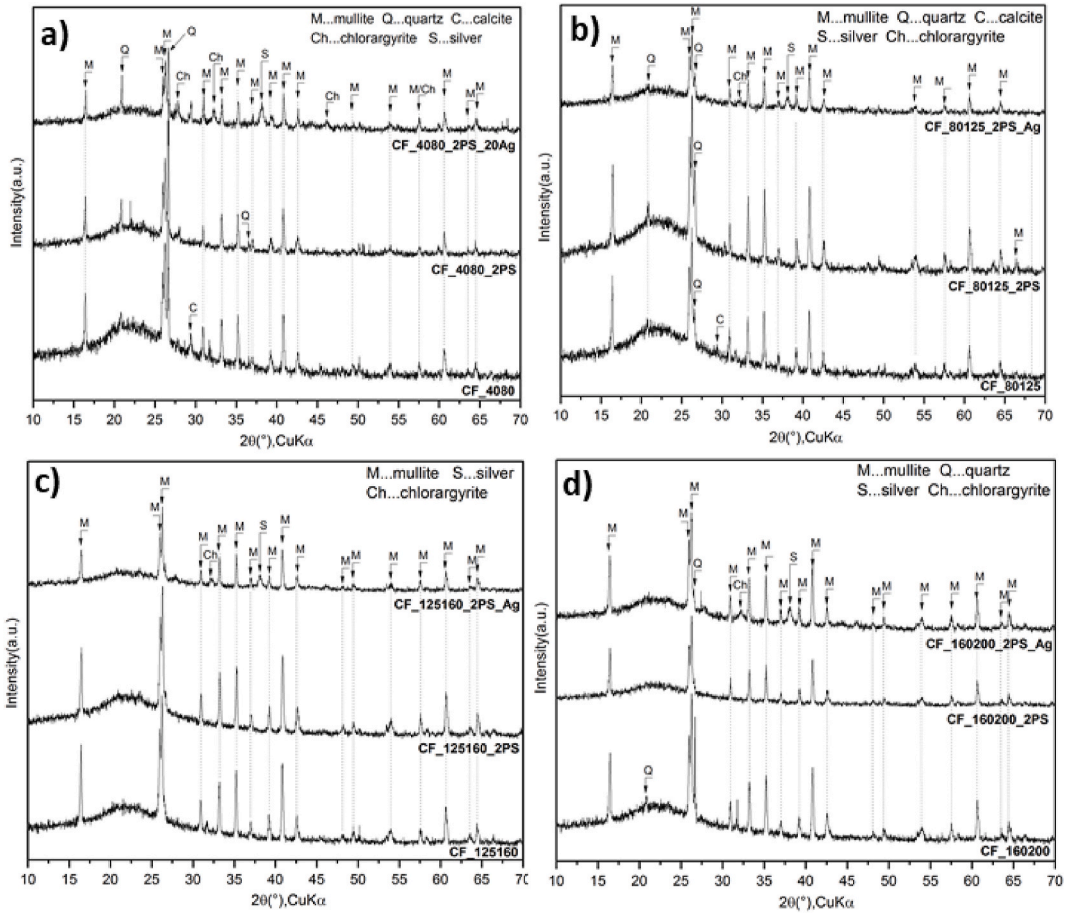

Fig. 2. XRD patterns of cenospheres samples arranged with relation to size fractions: a) 40–80 μm, b) 80–125 μm, c) 125–160 μm, d) 160–200 μm.

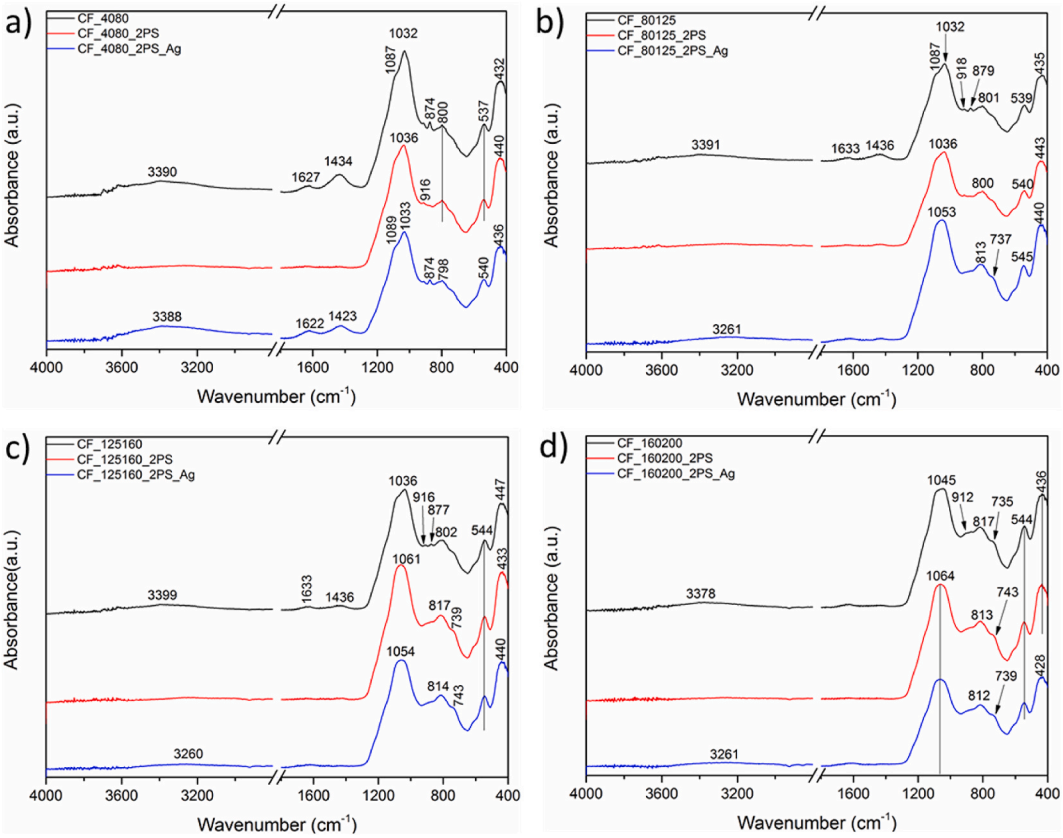

Fig. 3. FTIR spectra of cenospheres samples arranged with relation to size fractions: a) CF 40–80 μm, b) CF 80–125 μm, c) CF 125–160 μm, d) CF 160–200 μm (black lines– pure CF; red lines – CF after PS solution, blue lines – CF after PS and with Ag nanoparticles). (For interpretation of the references to colour in this figure legend, the reader is referred to the Web version of this article.)

4.2. Morphology of cenospheres and silver nanoparticles distribution

Fig. 4 shows electron microscope images of all prepared CF fractions – input (A-D), purified with pirhana solution (F-H) and mixed with nanosilver (I-L). The differences between the size fractions are obvious, as well as the effect of purification and etching with a mixture of sulfuric acid and hydrogen peroxide, after which the surface of the CF was more exposed and the internal structures were also revealed. At applied magnification, silver nanoparticles cannot be observed, however, the effect of stabilizing organic phyto-components caused a slight charging of the CF during the observation in the microscope chamber.

The silver nanoparticles are polydisperse with an average size of 45 nm (Fig. 5a, scale 100 nm). To better visualize the silver nanoparticles distributed on the surface of CF, material contrast in the backscattered electron mode (COMPO) was used. It is evident from the electron images that nanosilver does not decorate the CF evenly, but rather accumulates in places of structural defects (Fig. 5b, scale 10 μm), or leaves a ring after drying the sample (Fig. 5c, scale 10 μm). Nanoparticles occur on the surface of the CF individually, as larger agglomerated formations (Fig. 5d, scale 100 nm) or in thicker layers (Fig. 5e, scale 10 μm). They are occasionally found free outside the CF. These silver nanoparticles will probably release more easily into the surrounding solution during stability leaching tests (Fig. 5f, scale 1 μm). The images demonstrate distinct, irregular crystallization patterns forming a dense network of crystallites—small, ordered regions with sharply defined grain boundaries. These crystallites appear as closely packed, polygonal forms, creating a compact, granular structure.

In the EDS map sum spectrum of CF decorated with nanosilver (Fig. 6), the main elements from the CF composition were identified as Al (8.3 wt%), Si (6.3 wt%) and O (51.7 wt%). The contribution to the total Al content is attributed to the sample holder and Cu (1.3 wt%) from the used Cu-grid for STEM observation of silver nanoparticles. Gold was used to increase the conductivity of the sample for better observation in the electron microscope chamber. Along with silver (0.5 wt%), Cl (0.1 wt%), which is often an anthropogenic impurity in plant precursors, and C from organic material of plant origin (31.6 wt%) can also be identified. Accompanying elements in the CF composition can also be Fe and Ti (both 0.1 wt%). Chemical elements with low molecular weight such as C and O are quantitatively overestimated in the EDS analysis, which is evidenced by the higher standard deviation.

The results of true density measurements, obtained using He pycnometry, are summarized in Table 2. These findings reveal a consistent increase in density for all cenosphere fractions after modification. The incorporation of silver nanoparticles led to the most significant increase, with density values more than doubling for the 40–80 μm and 80–125 μm fractions compared to the original samples. Curiously the smallest and largest particle size fractions are showing similar values, however this phenomenon is caused by relatively similar porosity of large spherical particles (holes in the spheres and space around) and space around the fraction of the spheres and small spheres.

4.3. Sound absorption measurements

In general, sound absorption properties of loose powders are influenced by different factors, such as their density, particles' shape and size, porosity, thickness of the studied material layer and compressibility.

The effect of the particle size on the frequency dependencies of the sound absorption coefficient of the investigated unconsolidated loose powders of a given powder bed height is depicted in Fig. 7. The noise reduction coefficient (*NRC*) and the mean sound absorption coefficient (α_m) were subsequently evaluated based on these frequency dependencies.

The results of these coefficients depending on the powder height (h)

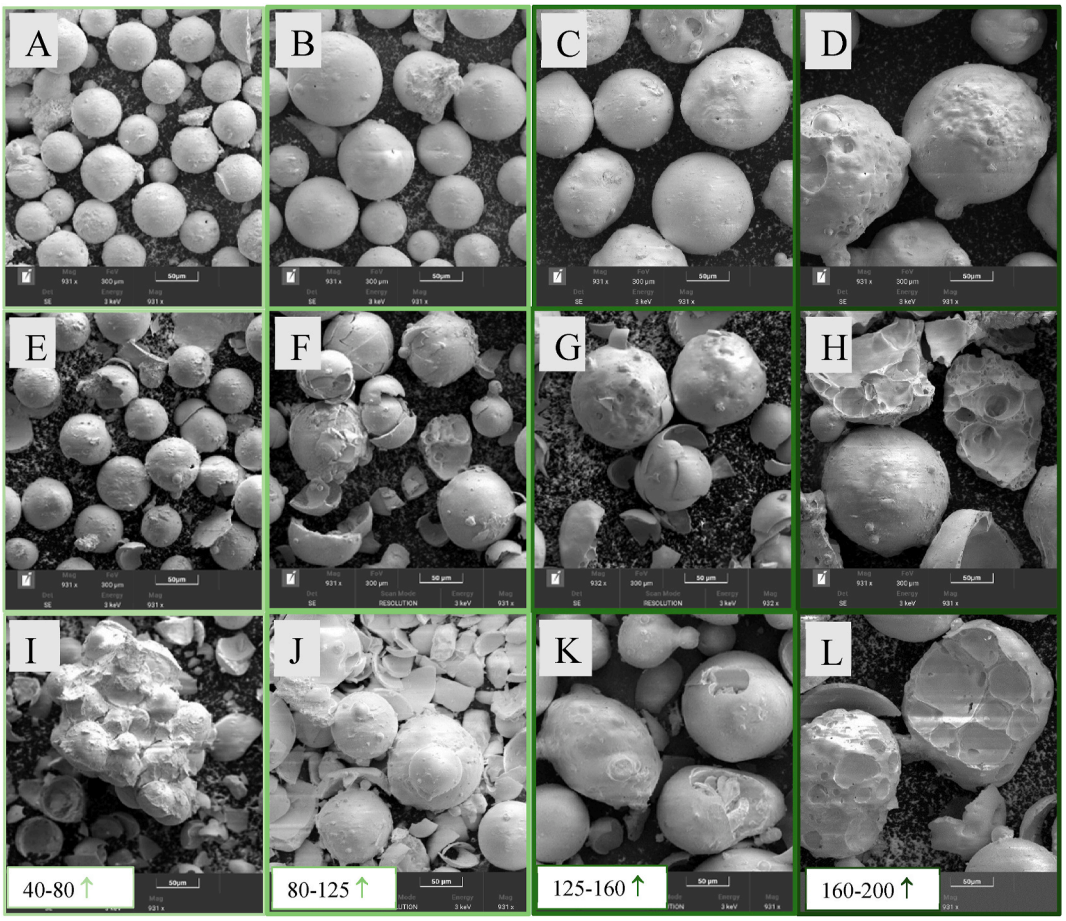

Fig. 4. Electron images document the morphology and size of the CF – input samples (A–D); etched in pirhana solution (E–H); mixed with bioreduced silver nanoparticles (I–L) for all prepared size fractions – 40–80 μm (A, E, I); 80–125 μm (B, F, J); 125–160 μm (C, G, K) and 160–200 μm (D, H, L); scale 50 μm.

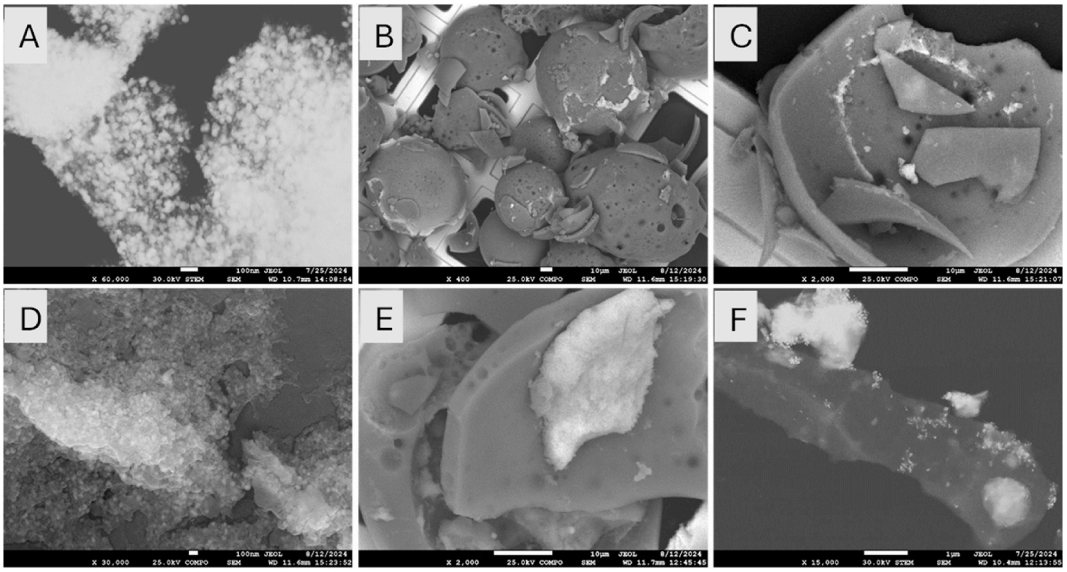

Fig. 5. Size and morphology of silver nanoparticles prepared via bioreduction with Verbena plant extract (5A, scale 100 nm, STEM regime); silver-based nanoparticles decorate the surface of CF-fragments after PS treatment (5B-F).

for the studied CF powders are presented in Tables 3 and 4. It was found based on these results that the particle size had a significant effect on *NRC* and α_m for the raw CF powders as shown in Table 3. It can be concluded that the sound absorption properties (i.e., the coefficients *NRC* and α_m) generally increased with increasing the particle size of the investigated raw CF. This phenomenon is mainly related to the porosity of powder materials.

As a result, sound waves are more likely to be reflected between

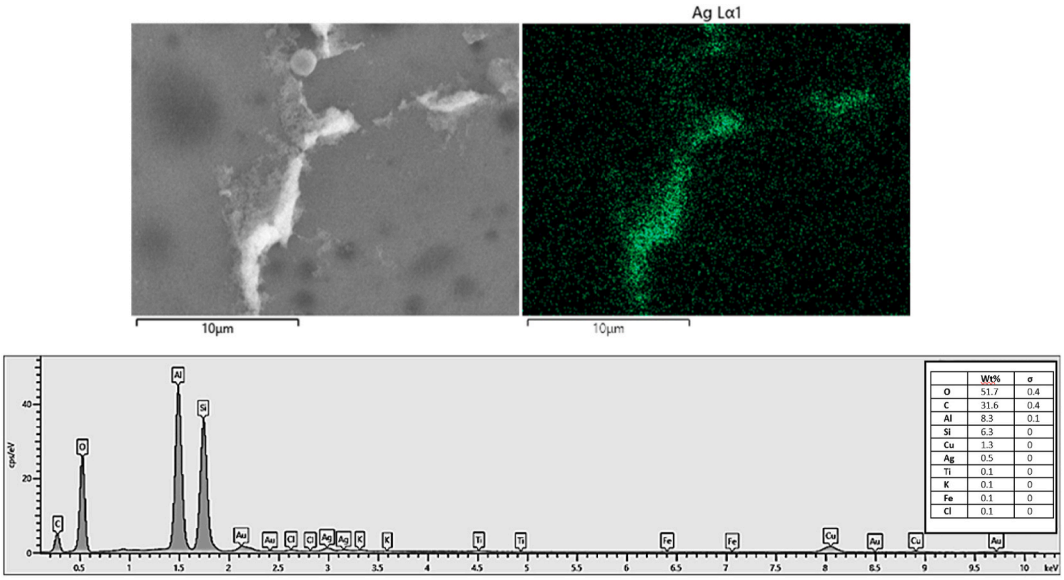

Fig. 6. Nanocrystalline silver layer deposited on the surface of the cenosphere with silver EDS map and summary EDS spectrum.

Table 2
True density measurement results of CF samples.

Sample	Density, g/cm^3
CF_4080	1.0224
CF_4080_ 2 PS	1.1420
CF_4080_2 PS_Ag	1.4391
CF_80125	0.6118
CF_80125_2 PS	1.0314
CF_80125_2 PS_Ag	1.4300
CF_125160	0.7523
CF_125160_2 PS	1.1463
CF_125160_2PSAg	1.4664
CF_160200	1.0572
CF_160_200_2 PS	1.1800
CF_160200_2 PS_Ag	1.5710

particles, which increases the conversion of acoustic energy into heat and increases the sound absorption of powder materials with larger particle sizes. Different sound absorption properties were observed after the addition of Ag nanoparticles to the raw CF powders. Again, the lowest values of *NRC* and α_m coefficients were found for the modified Ag CF powders with particle sizes in the range of 40–80 μm. For other particle sizes, the sound absorption behaviour of the modified Ag CF powders was very similar, so that the effect of particle size on the *NRC* and α_m coefficients was negligible, as shown in Table 4.

The effect of powder bed height h on the sound absorption properties of two types of loose CF powders is shown in Fig. 8. It is evident that powder bed height had a significant influence on the primary absorption peak frequency (f_{p1}), which generally decreased as the powder bed height increased, as shown in Tables 3 and 4 However, the powder bed height of the unconsolidated CF powders had a negligible influence on their overall sound absorption properties.

It was found based on the calculated α_m values (see Tables 3 and 4) that raw CF powders with particle sizes in the range of 160–200 μm exhibited a higher ability to absorb sound compared to the modified Ag CF powders across almost the entire range of powder bed heights. Conversely, the modified Ag CF powders with smaller particle sizes (i.e., from 40 to 125 μm) demonstrated better sound absorption properties than the raw CF powders over a substantial range of powder bed heights.

Finally, the experimentally measured frequency dependencies of the sound absorption coefficient α were used to determine the velocity (c) of the longitudinal elastic wave propagating through the powder bed and the longitudinal elasticity coefficient (K) of the investigated CF powders. These quantities were calculated based on the obtained values of the primary absorption peak frequency f_{p1} (see Figs. 7 and 8) and the bulk density (ρ_b) according to Equation (3). Their values for various powder bed heights are given in Tables 3 and 4 As shown in Fig. 9, the longitudinal elasticity coefficient (K), and thus the mechanical stiffness of the

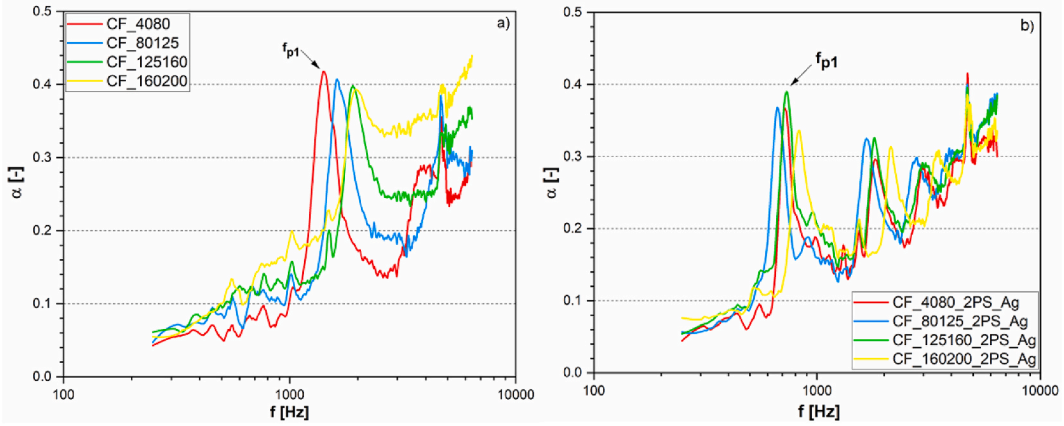

Fig. 7. Frequency dependencies of the sound absorption coefficient: a) for raw CF powders with a bed height of 10 mm, b) for modified Ag CF powders with a bed height of 25 mm.

Table 3
Results of the calculated and measured acoustical and mechanical quantities of studied raw CF powders at selected powder bed height *h*.

Sample	Quantity	*h* (mm)						
		5	10	15	25	30	50	80
CF_4080	fp_1 (Hz)	2520	1400	1168	736	704	664	552
	NRC (−)	0.084	0.088	0.121	0.136	0.106	0.103	0.146
	α_m (−)	0.203	0.218	0.212	0.219	0.202	0.199	0.226
	c (m/s)	50.4	56.0	70.1	73.6	84.5	132.8	176.6
	K (MPa)	2.60	3.21	5.02	5.54	7.30	18.03	31.90
CF_80125	fp_1 (Hz)	3080	1608	1176	816	784	736	664
	NRC (−)	0.066	0.130	0.127	0.158	0.155	0.131	0.108
	α_m (−)	0.217	0.233	0.223	0.220	0.223	0.230	0.228
	c (m/s)	61.6	64.3	70.6	81.6	94.1	147.2	212.5
	K (MPa)	2.32	2.53	3.05	4.07	5.42	13.26	27.62
CF_125160	fp_1 (Hz)	3344	1936	1456	1000	952	832	832
	NRC (−)	0.084	0.171	0.129	0.182	0.166	0.136	0.129
	α_m (−)	0.259	0.258	0.252	0.265	0.250	0.257	0.244
	c (m/s)	66.9	77.4	87.4	100.0	114.2	166.4	266.2
	K (MPa)	3.36	4.51	5.74	7.52	9.82	20.83	53.33
CF_160200	fp_1 (Hz)	4752	1976	1632	1096	920	904	872
	NRC (−)	0.086	0.180	0.182	0.193	0.205	0.194	0.210
	α_m (−)	0.291	0.319	0.319	0.320	0.336	0.313	0.351
	c (m/s)	95.0	79.0	97.9	109.6	110.4	180.8	279.0
	K (MPa)	9.55	6.60	10.14	12.70	12.89	34.56	82.32

Table 4
Results of the calculated and measured acoustical and mechanical quantities of studied modified Ag CF powders at selected powder bed heights *h*.

Sample	Quantity	*h* (mm)						
		5	10	15	25	30	50	80
CF_4080_2 PS_Ag	fp_1 (Hz)	2312	1360	1012	712	696	580	560
	NRC (−)	0.116	0.120	0.151	0.132	0.104	0.110	0.143
	α_m (−)	0.226	0.229	0.248	0.248	0.228	0.217	0.247
	c (m/s)	46.2	54.4	60.7	71.2	83.5	116.0	177.3
	K (MPa)	3.08	4.26	5.31	7.30	10.04	19.36	45.23
CF_80125_2 PS_Ag	fp_1 (Hz)	2216	1376	936	656	656	552	554
	NRC (−)	0.131	0.096	0.147	0.129	0.132	0.182	0.159
	α_m (−)	0.253	0.225	0.260	0.270	0.262	0.287	0.291
	c (m/s)	44.3	55.0	56.2	65.6	78.7	110.4	177.3
	K (MPa)	2.81	4.33	4.51	6.15	8.86	17.43	44.94
CF_125160_2 PS_Ag	fp_1 (Hz)	2656	1384	1032	744	696	632	600
	NRC (−)	0.075	0.127	0.160	0.145	0.142	0.135	0.151
	α_m (−)	0.233	0.265	0.262	0.269	0.278	0.251	0.283
	c (m/s)	53.1	55.4	61.9	74.4	83.5	126.4	192.0
	K (MPa)	4.14	4.49	5.62	8.12	10.23	23.43	54.06
CF_160200_2 PS_Ag	fp_1 (Hz)	2496	1504	1144	824	752	672	632
	NRC (−)	0.096	0.120	0.151	0.154	0.148	0.151	0.158
	α_m (−)	0.254	0.232	0.269	0.254	0.266	0.280	0.279
	c (m/s)	49.9	60.2	68.6	82.4	90.2	134.4	202.2
	K (MPa)	3.91	5.69	7.40	10.67	12.79	28.38	64.26

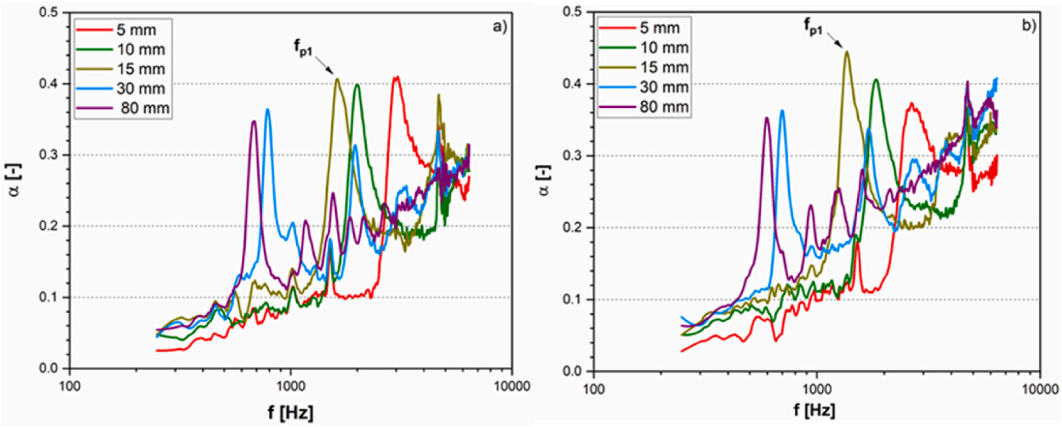

Fig. 8. Frequency dependencies of the sound absorption coefficient for different loose powder beds heights: a) for raw CF powders with fractions of 80–125 μm, b) for modified Ag CF powders with fractions of 160–200 μm.

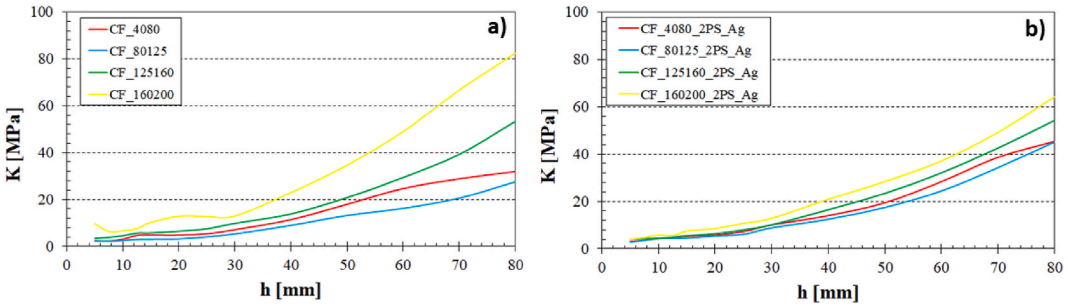

Fig. 9. Effect of the loose powder bed height on the longitudinal elastic coefficient: a) for raw CF powders with different fractions, b) for modified Ag CF powders with different fractions.

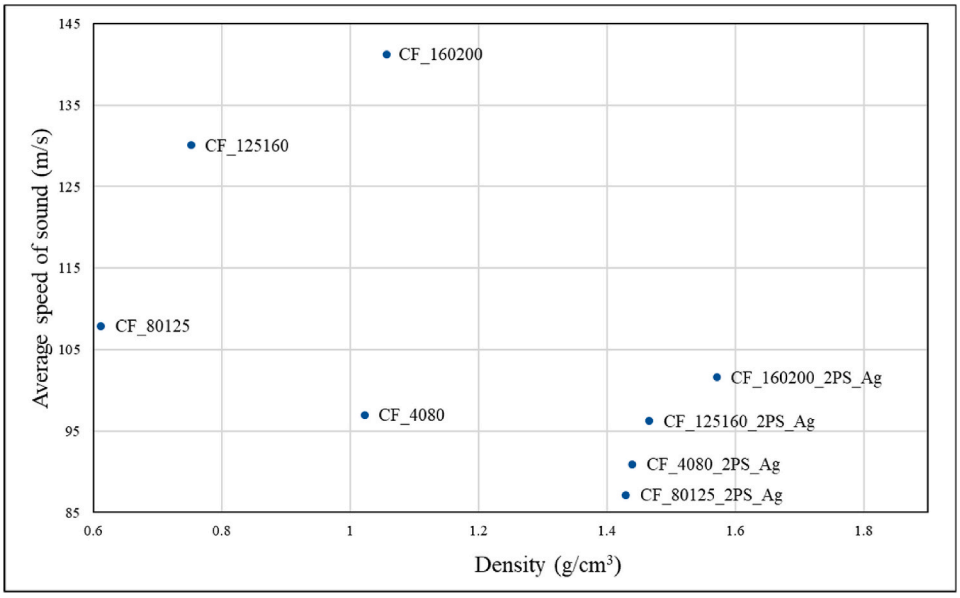

Fig. 10. Comparison of average values of sounds speed vs true density of all samples.

CF powders, generally increased with powder bed height. Higher mechanical stiffness was observed for both raw CF and modified Ag CF powders containing the largest particles (i.e., from 160 to 200 μm). Conversely, the lowest mechanical stiffness was found in both types of CF powders with particle sizes ranging from 80 to 125 μm. From the comparison of both types of the investigated loose powders (see Fig. 9a and b), it is clear that higher mechanical stiffness was generally found for the modified Ag CF powders. Only in the case of powders containing the largest particle sizes (i.e., from 160 to 200 μm), the raw CF powders exhibited higher values of the longitudinal elasticity coefficient, and thus higher mechanical stiffness, compared to the modified Ag CF powders. The bulk modulus *K*, indicating material stiffness, shows a clear positive correlation with density. High-density samples (e.g., CF_160200_2 PS_Ag with 64.26 MPa) generally exhibited significantly higher mechanical stiffness compared to low-density ones (e.g., CF_80125 with 27.62 MPa).

Higher density materials (e.g., CF_160200_2 PS_Ag with 1.571 g/cm^3) are generally characterized by higher *NRC* values, indicating better sound absorption. Lower density materials (e.g., CF_80125 with 0.6118 g/cm^3) exhibited lower *NRC* values, suggesting less efficient sound absorption. The average speed of sound (see Fig. 10) was generally higher in denser samples (e.g., CF_160200_2 PS_Ag with 101.6 m/s) compared to lower-density ones (e.g., CF_80125_2 PS_Ag with 87.1 m/s). Dense materials tend to be stiffer, which accelerates sound wave propagation. It can also be concluded that the decoration of the CF with Ag resulted in a reduction in the speed of sound, as shown in Fig. 10.

4.4. Stability testing of decorated CF

One of the main goals was both the preparation of a functional material with the required properties and its stability in the environment in which it will be applied. Therefore, the leachability test under static and dynamic conditions was used to determine the stability of decorated CF materials.

The percentage of Ag released from CF_4080_2 PS_Ag, CF_125160_2 PS_Ag and CF_160200_2 PS_Ag samples to the leachates after the static (S) leaching test were comparable (see Fig. 11). A slightly higher amount of Ag was released from CF_80125_2 PS_Ag, which also corresponds with higher amounts of released Al, Fe, and Mg compared to other CF samples (Table 5). This could be due to the lowest density of CF_80125 (1.43 g/cm^3) compared to the other CF Ag decorated samples (see Table 3) as the distilled water probably affected the surface and pores more intensively.

The leaching test under dynamic conditions (D) did not significantly affect the release of Ag from sample CF_4080_2 PS_Ag compared to CF_80125_2 PS_Ag, CF_125160_2 PS_Ag and CF_160200_2 PS_Ag where the Ag concentrations released under dynamic conditions were higher. The amount of Ag released from CF_80125_2 PS_Ag, CF_125160_2 PS_Ag and CF_160200_2 PS_Ag samples in the dynamic (D) leaching test were not significantly different. Compared to the previous static (S) test, the dynamic leaching test also had no significant effect on the release of the monitored elements from the CF materials.

The dependence was observed after the rotation (R) leaching test. The proportion of Ag released into the leachates obtained by rotation test (R) increased with increasing fraction size. Even when dynamic conditions were used during the leachability test, there was no

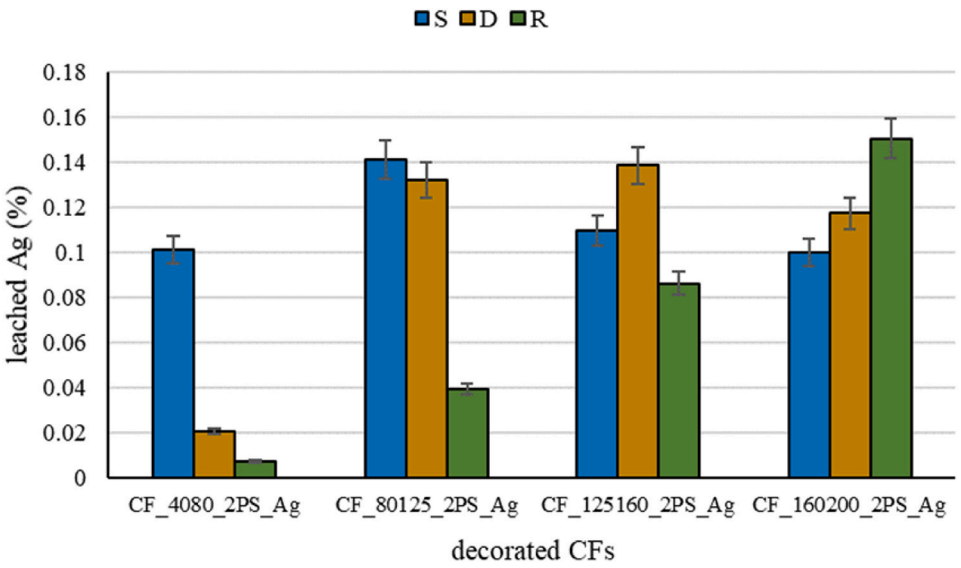

Fig. 11. The percentage of Ag leached from CF_4080_2 PS_Ag, CF_80125_2 PS_Ag, CF_125160_2 PS_Ag and CF_160200_2 PS_Ag under static (S), dynamic (D) and rotation (R) conditions.

Table 5
The amount (in wt.%) of selected elements released from CF samples after static (S), dynamic (D) and rotational (R) leaching tests.

	Ag (wt.%)	Al (wt.%)	Ca (wt.%)	Fe (wt.%)	K (wt.%)	Mg (wt.%)	Si (wt.%)
S_CF_4080		0.003	0.344	0.002	0.010	0.030	0.012
S_CF_4080_2 PS_Ag	0.006	0.002	0.310	0.001	0.017	0.030	0.008
S_CF_80125_2 PS_Ag	0.009	0.012	0.016	0.003	0.012	0.007	0.005
S_CF_125160_2 PS_Ag	0.008	0.008	0.007	0.001	0.007	0.003	0.002
S_CF_160200_2 PS_Ag	0.007	0.009	0.009	0.001	0.008	0.004	0.010
D_CF_40_80		0.002	0.332	<0.500	0.010	0.029	0.012
D_CF_4080_2 PS_Ag	0.001	0.002	0.302	<0.500	0.016	0.028	0.008
D_CF_80125_2 PS_Ag	0.008	0.011	0.015	0.002	0.008	0.006	0.005
D_CF_125160_2 PS_Ag	0.010	0.008	0.017	0.002	0.007	0.006	0.004
D_CF_160200_2 PS_Ag	0.008	0.009	0.016	0.002	0.015	0.003	0.003
R_CF_40_80		0.001	0.366	<0.500	0.007	0.028	0.013
R_CF_4080_2 PS_Ag	0.001	0.001	0.358	<0.500	0.021	0.032	0.009
R_CF_80125_2 PS_Ag	0.002	0.010	0.021	0.002	0.015	0.004	0.002
R_CF_125160_2 PS_Ag	0.006	0.010	0.016	0.003	0.014	0.006	0.011
R_CF_160200_2 PS_Ag	0.010	0.008	0.009	0.001	0.008	0.003	0.003

significant release of Ag from the CF samples tested. Even in the rotation leaching test, the monitored elements did not loosen significantly more than in the previous S and D tests.

In general, the highest amounts of released alkaline elements (Ca, K and Mg) were determined in the leachates (S, D and R) obtained from the material with the lowest size fraction CF_4080_2 PS_Ag than from the CF_80125_2 PS_Ag, CF_125160_2 PS_Ag and CF_160200_2 PS_Ag. This may be related to the small particle size and the relative ease of release of these elements into the aqueous environment. While Al and Fe are mainly released from materials with a larger fraction of particle size (Table 5).

It can be concluded that Ag is firmly attached to the CF surface, selected elements have not been released significantly and, therefore, the CF materials can be considered stable under the stated conditions.

5. Conclusions

Studied cenosphere powder samples were compared for all possible combined effects of stability and materials characteristics. The static stability test provides a controlled, predictable environment suitable for analyzing the stability and equilibrium behavior of sorbent materials. The dynamic stability test offers insights into the performance under agitation or movement, emphasizing mobilization and release rates. For larger fractions, greater silver release was observed under rotational conditions, which may suggest less stability of these samples under dynamic conditions. Each process affects the stability of the samples in solution differently, which may be important when choosing the appropriate method to test the stability of materials in different environments. However, after stability tests, silver nanoparticles remain on the cenospheres. Despite this, studies indicate good stability of cenospheres under static conditions, suggesting that modified cenospheres may be effective in long-term environmental clean-up applications without excessive release of silver into water. Thanks to the modification of cenospheres with silver nanoparticles, a cover of organic compounds remains, which in the future may provide also a catalytic effect and exhibit electrical properties. This study also presented a non-destructive sound absorption test to evaluate both the sound absorption properties and mechanical stiffness of bulk powders. The results indicate that CF samples with larger particle sizes exhibited a higher ability to absorb sound. The mechanical stiffness of the studied CF, characterized by the bulk modulus, significantly increased with powder bed height and density. For these reasons, the highest sound absorption (α_{mmax} = 0.351) and mechanical stiffness (K_{max} = 82.32 MPa) were obtained for the CF_160200 sample with the maximum powder bed height (h_{max} = 80 mm). Additionally, CF decorated with silver nanoparticles generally exhibited higher mechanical stiffness compared to raw CF. In summary, the study demonstrates that silver-modified cenospheres exhibit favorable structural stability, limited silver leaching under various environmental conditions, and enhanced functional properties. Their improved sound absorption performance, increased

mechanical stiffness, and potential catalytic activity make them promising candidates for applications in environmental remediation, acoustic insulation, and multifunctional composite materials.

CRediT authorship contribution statement

Magdalena Antonowicz: Writing – review & editing, Writing – original draft, Visualization, Validation, Software, Resources, Methodology, Investigation, Formal analysis, Data curation. **Jana Kupková:** Writing – review & editing, Writing – original draft, Visualization, Validation, Software, Resources, Methodology, Investigation, Formal analysis, Data curation. **Gabriela Kratošová:** Writing – review & editing, Visualization, Resources, Project administration, Methodology, Investigation, Formal analysis, Data curation, Conceptualization. **Lenka Klecandová:** Visualization, Software, Investigation, Formal analysis. **Martin Vašina:** Writing – original draft, Investigation, Formal analysis. **Justyna Majewska:** Investigation. **Michaela Tokarčíková:** Software, Investigation, Formal analysis. **Grazyna Simha Martynková:** Writing – review & editing, Validation, Supervision, Project administration, Methodology, Funding acquisition, Conceptualization.

Availability of data and materials

The data that support the findings of this study are openly available in repository ZENODO at https://doi.org/10.5281/zenodo.14272437 [39].

Declaration of competing interest

The authors declare that they have no known competing financial interests or personal relationships that could have appeared to influence the work reported in this paper.

Acknowledgements

This paper was created as part of the project No. CZ.02.01.01/00/22_008/0004631. Materials and technologies for sustainable development within the Jan Amos Komensky Operational Program financed by the EU and state budget of the Czech Republic and was prepared with the financial support of the EU under the REFRESH – project number CZ.10.03.01/00/22_003/0000048 via the Operational Programme Just Transition.

Appendix

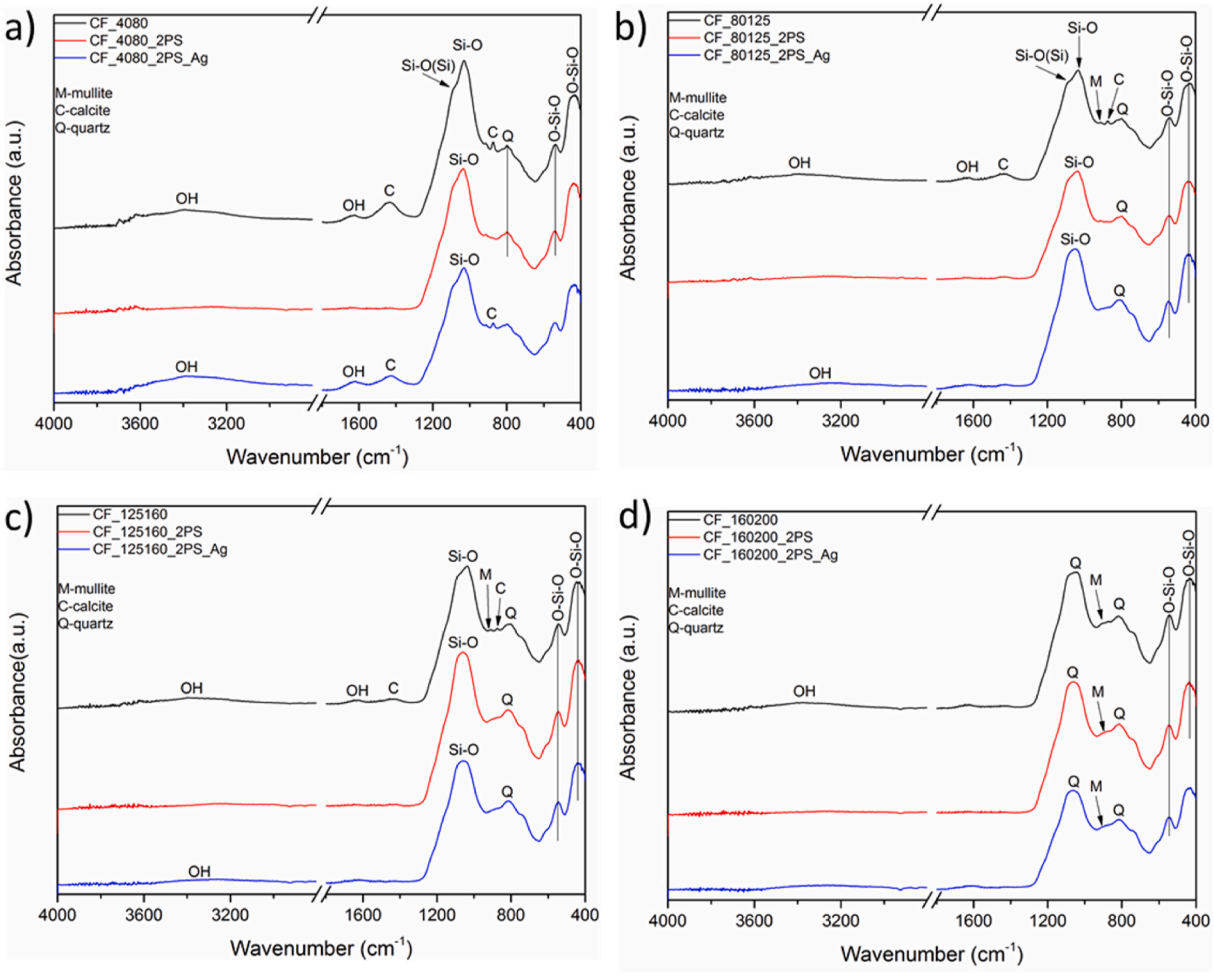

Attachement:

References

[1] D.S. Nakonieczny, M. Antonowicz, Z. Paszenda, Surface modification methods of ceramic filler in ceramic-carbon fibre composites for bioengineering applications – a systematic review, Rev. Adv. Mater. Sci. 59 (2020) 586–605, https://doi.org/10.1515/rams-2020-0024.

[2] N. Ranjbar, C. Kuenzel, Cenospheres: a review, Fuel 207 (2017) 1–12, https://doi.org/10.1016/j.fuel.2017.06.059.

[3] V.K. Yadav, K.K. Yadav, N. Choudhary, et al., Recent advances in methods for recovery of cenospheres from fly ash and their emerging applications in ceramics, composites, polymers, and environmental cleanup, Crystals 11 (2021), https://doi.org/10.3390/cryst11091067.

[4] A.D. Johar, H. Mohamed, Z. Itam, N.M. Zahari, Z.C. Muda, A. Syamsiret, et al., A review on methods of cenosphere separation from fly ash, Appl. Mech. Mater. 919 (2024) 57–65, https://doi.org/10.4028/p-q3damx.

[5] H. Zhang, W. Ma, F. Gao, Z. Ge, M. Yang, H. Fang, et al., Rheology, shrinkage, mechanical properties and microstructure of ultra-light-weight concrete with fly ash cenospheres, J. Build. Eng. 98 (2024) 111258, https://doi.org/10.1016/j.jobe.2024.111258.

[6] A. Danish, M.A. Mosaberpanah, R. Tuladhar, et al., Effect of cenospheres on the engineering properties of lightweight cementitious composites: a comprehensive review, J. Build. Eng. 49 (2022), https://doi.org/10.1016/j.jobe.2022.104016.

[7] T.F. Choo, M.A. Mohd Salleh, K.Y. Kok, K.A. Matori, Modified cenospheres as non-sacrificial pore-forming agent for porous mullite ceramics, Ceram. Int. 45 (2019) 21827–21834, https://doi.org/10.1016/j.ceramint.2019.07.189.

[8] E. Strzałkowska, Z. Adamczyk, Influence of chemical composition of fly-ash cenospheres on their grain size, Int. J. Environ. Sci. Technol. 17 (2020) 809–818, https://doi.org/10.1007/s13762-019-02512-2.

[9] Y. Yi, C. Li, Y. Han, J. Nie, C. Fan, Q. He, Preparation and sound absorption performance of low-carbon fly ash cenosphere plates, Int. J. Ceramic. Eng. Sci. (2024), https://doi.org/10.1002/ces2.10204.

[10] M. Tiwari, S.P. Shukla, D. Mohan, D.S. Bhargava, G.C. Kisku, Modified cenospheres as an adsorbent for the removal of disperse dyes, Adv. Environ. Chem. 2015 (2015) 349254, https://doi.org/10.1155/2015/349254.

[11] J.C. Ge, S.K. Yoon, N.J. Choi, Application of fly ash as an adsorbent for removal of air and water pollutants, Appl. Sci. 8 (2018) 1116, https://doi.org/10.3390/app8071116.

[12] Uyiosa Osagie Aigbe, et al., Fly ash-based adsorbent for adsorption of heavy metals and dyes from aqueous solution: a review, J. Mater. Res. Technol. 14 (2021) 2751–2774, https://doi.org/10.1016/j.jmrt.2021.07.140.

[13] O.A. Fedyaeva, E.G. Poshelyuzhnaya, Investigation of interactions in the cenospheres-electrolyte system, J. Phys. Conf. Ser. 1546 (2020), https://doi.org/10.1088/1742-6596/1546/1/012116.

[14] D.S. Nakonieczny, M. Antonowicz, T. Heim, et al., Cenospheres-reinforced PA-12 composite: preparation, physicochemical properties, and soaking tests, Polymers 14 (2022), https://doi.org/10.3390/polym14122332.

[15] N. Tarasova, M. Khanov, D. Vorobiev, et al., Fly-ash cenosphere as non-porous Ag-nanoparticle support for epoxidation of styrene, ChemistrySelect 9 (2024) e202401003, https://doi.org/10.1002/slct.202401003.

[16] K. Sukhareva, I. Burmistrov, E. Mamin, et al., Effects of neat and silver-coated fly ash cenospheres on the properties of styrene-butadiene-styrene block copolymer composites obtained by a solution mixing method, J. Elastomers Plast. 56 (2024) 745–773, https://doi.org/10.1177/00952443241268637.

[17] V. Gadore, M. Ahmaruzzaman, Tailored fly ash materials: a recent progress of their properties and applications for remediation of organic and inorganic contaminants from water, J. Water Process Eng. 41 (2021), https://doi.org/10.1016/j.jwpe.2020.101910.

[18] C. Ni, C. Liu, Y. Xie, et al., A critical review on adsorption and recovery of fluoride from wastewater by metal-based adsorbents, Environ. Sci. Pollut. Res. 29 (2022) 82740–82761, https://doi.org/10.1007/s11356-022-23416-8.

[19] Markandeya, S.P. Shukla, A.L. Srivastav, Removal of disperse orange and disperse blue dyes present in textile mill effluent using zeolite synthesized from cenospheres, Water Sci. Technol. 84 (2021) 445–457, https://doi.org/10.2166/wst.2021.216.

[20] G. Kratosova, V. Holesova, Z. Konvickova, et al., From biotechnology principles to functional and low-cost metallic bionanocatalysts, Biotechnol. Adv. 37 (2019) 154–176, https://doi.org/10.1016/j.biotechadv.2018.11.012.

[21] T.M.-T. Nguyen, T.T.-T. Huynh, C.H. Dang, et al., Novel biogenic silver nanoparticles used for antibacterial effect and catalytic degradation of contaminants, Res. Chem. Intermed. 46 (2020) 1975–1990, https://doi.org/10.1007/s11164-019-04075-w.

[22] M. Rai, A.P. Ingle, J. Trzcinska-Wencel, et al., Biogenic silver nanoparticles: what we know and what do we need to know? Nanomaterials 11 (2021) https://doi.org/10.3390/nano11112901.

[23] O. Nejati, G. Torkay, A. Girgin, et al., Biocompatible silver nanoparticles from apricot kernel skin: a green synthesis approach to antibacterial and antiangiogenic therapies, Chem. Pap. (2024), https://doi.org/10.1007/s11696-024-03793-9.

[24] K. Sharma, G. Singh, M. Kumar, V. Bhalla, Silver nanoparticles: facile synthesis and their catalytic application for the degradation of dyes, RSC Adv. 5 (2015) 25781–25787, https://doi.org/10.1039/C5RA02909K.

[25] J.M. Sasikumar, A. Salahadin, C.E. Meseret, P.R. Jeyaramraja, S. Balakrishnan, Green synthesis of silver nanoparticles from verbena officinalis l.: characterization and antibacterial efficacy, Plant Sci. Today (2025), https://doi.org/10.14719/pst.5061.

[26] Z. Konvickova, K.C. Barabaszova, V. Holisova, et al., Phytosynthesis of Ag, ZnO and ZrO_2 nanoparticles using linden: changes in their physical-chemical nature over time, J. Nanosci. Nanotechnol. 19 (2019) 7926–7933, https://doi.org/10.1166/jnn.2019.15854.

[27] S. Pakseresht, A.W. Alogaili, H. Akbulut, et al., Silver/chitosan antimicrobial nanocomposites coating for medical devices: comparison of nanofiller effect prepared via chemical reduction and biosynthesis, J. Nanosci. Nanotechnol. 19 (2019) 2938–2942, https://doi.org/10.1166/jnn.2019.15854.

[28] X. Tang, X. Yan, Acoustic energy absorption properties of fibrous materials: a review, Compos. Appl. Sci. Manuf. 101 (2017) 360–380, https://doi.org/10.1016/j.compositesa.2017.07.002.

[29] E.S. Jang, The performance of interior building sound-absorbing material of cross-sectional oak (*Quercus* spp.) in combination with disposable mask waste (DMW), Appl. Acoust. 216 (2024) 109802, https://doi.org/10.1016/j.apacoust.2023.109802.

[30] Y. Okudaira, Y. Kurihara, H. Ando, M. Satoh, K. Miyanami, Sound absorption measurements for evaluating dynamic physical properties of a powder bed, Powder Technol. 77 (1) (1993) 39–48, https://doi.org/10.1016/0032-5910(93)85005-T.

[31] International Organization for Standardization, ISO 10534-2, acoustics-determination of sound absorption coefficient and impedance in impedance tubes-Part 2: transfer-function method. ISO/TC 43/SC2 Building Acoustics; CEN, European Committee for Standardization, 1998.

[32] F. Han, G. Seiffert, Y. Zhao, B. Gibbs, Acoustic absorption behaviour of an open-celled aluminium foam, J. Phys. D Appl. Phys. 36 (3) (2003) 294, https://doi.org/10.1088/0022-3727/36/3/312.

[33] E.V. Fomenko, N.N. Anshits, L.A. Solovyov, O.A. Mikhaylova, A.G. Anshits, Composition and morphology of fly ash cenospheres produced from the combustion of Kuznetsk coal, Energy Fuels 27 (9) (2013) 5440–5448, https://doi.org/10.1021/ef400754c.

[34] Y. Liu, F. Zeng, B. Sun, P. Jia, I.T. Graham, Structural characterizations of aluminosilicates in two types of fly ash samples from Shanxi Province, North China, Minerals 9 (6) (2019) 358, https://doi.org/10.3390/min9060358.

[35] W. Mozgawa, M. Król, J. Dyczek, J. Deja, Investigation of the coal fly ashes using IR spectroscopy, Spectrochim. Acta Mol. Biomol. Spectrosc. 132 (2014) 889–894, https://doi.org/10.1016/j.saa.2014.05.052.

[36] M. Ritz, Infrared and Raman spectroscopy of mullite ceramics synthesized from fly ash and kaolin, Minerals 13 (7) (2023) 864, https://doi.org/10.3390/min13070864.

[37] S. Hajji, T. Turki, A. Boubakri, M. Ben Amor, N. Mzoughi, Study of cadmium adsorption onto calcite using full factorial experiment design, Desalination Water Treat. 83 (2017) 222–233, https://doi.org/10.5004/dwt.2017.21079.

[38] K. Čech Barabaszová, et al., Effect of milling atmosphere on stability and surface properties of ZnO/vermiculite hybrid nanocomposite powders, Surf. Interfaces 51 (2024) 104534.

[39] M. Antonowicz, J. Kupková, G. Kratošová, L. Klecandová, M. Vašina, J. Majewska, G. Simha Martynková, M. Tokarčíková, Decoration of Cenospheres Surface with Bioreduced Silver Nanoparticles for Environmental Applications, Zenodo, 2024.